Supporting Information

Nanomagnetism of Magnetoelectric Granular Thin-Film Antiferromagnets

Patrick Appel,[†,§] Brendan J. Shields,[†,§] Tobias Kosub,[‡,¶] Natascha Hedrich,[†] René Hübner,[‡] Jürgen Faßbender,[‡] Denys Makarov,[‡,¶] and Patrick Maletinsky[*,†]

†*Department of Physics, University of Basel, Klingelbergstrasse 82, Basel CH-4056, Switzerland*

‡*Helmholtz-Zentrum Dresden-Rossendorf e.V., Institute of Ion Beam Physics and Materials Research, 01328 Dresden, Germany*

¶*Institute for Integrative Nanosciences, Institute for Solid State and Materials Research (IFW Dresden e.V.), 01069 Dresden, Germany.*

§*These authors contributed equally*

E-mail: patrick.maletinsky@unibas.ch

1 NV magnetometry

Scanning NV magnetometry [1] was performed under ambient conditions, using single-crystal diamond scanning probes as described in .[2] For the measurements, a single NV center contained within the apex of the scanning probe was scanned within $\sim$ 100 nm of the Cr_2O_3 surface. For quantitative magnetometry, the electron spin resonance (ESR) frequency was recorded by locking a microwave driving field to the ESR transition.[3] For this, a green laser (power level $\sim$ 10 μW) was used to excite NV fluorescence, resulting in typical fluorescence count rates $\sim$ 700 kHz and ESR contrasts $\sim$ 15 %. In order to obtain a sign-sensitive measurement of B_{NV}, a bias magnetic field of 24 G was applied along the NV axis during all measurements. The single-pixel integration time for the measurements presented here ranges from 0.6 s (temperature cycling correlation images used in Fig. 4c,d) to 7 s (Fig. 2a).

The NV magnetometry procedure is non-invasive and does not alter the magnetic state of the sample. To verify this, we carried out repeated scans of the same sample area under ambient conditions for 9 hours (Fig. S1), over which time the magnetization pattern persists. (Note: sample drift of $\sim$ 30 nm/hr has not been corrected in these measurements).

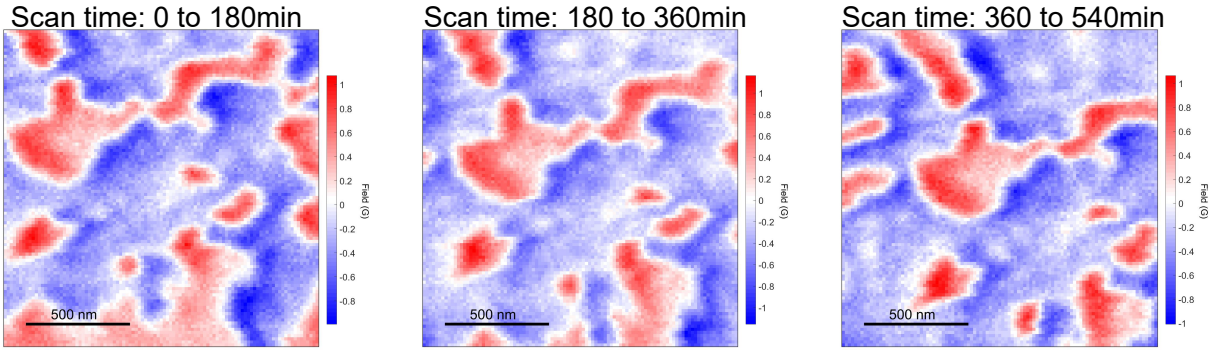

Figure S1: Repeated scans of the same sample area indicate minimal influence of the NV magnetometry procedure on the sample magnetization.

2 Zero-offset Hall magnetometry

We use Zero-offset Hall magnetometry (ZOHM) to study the average magnetization of the film within the 900 µm^2 area of a Pt hall cross patterned on the top surface of the Cr_2O_3 film.[4] In order to study tiny anomalous Hall signals, it is mandatory to dynamically reject the influence of the longitudinal resistance, which, even for carefully patterned Hall cross structures, can be much larger than the Hall signal of interest. While this is elegantly achieved using the ZOHM scheme, the normal Hall effect cannot be rejected using this approach. We remove the normal Hall effect after the measurement by subtracting it from the measured transverse resistance. The observed normal Hall effect is not completely linear in the magnetic field for two reasons: a) our magnetic field reading is not fully linear over the actual magnetic field mainly due to nonlinearities of the Si hall probe, and b) the normal Hall effect of the thin Pt film can be slightly non-linear itself. These influences cause a total nonlinearity of the normal Hall effect in the range of 10^{-2} to 10^{-3}, which is not relevant considering the strength of the anomalous Hall signal measured on the samples.

3 Sample fabrication

The Cr_2O_3 films were grown by reactive evaporation of chromium from a Knudsen cell in high vacuum onto *c*-cut sapphire substrates (Crystec GmbH) heated to 700 °C initially and to 500 °C after the first few monolayers. The background gas used was molecular oxygen at a partial pressure of 10^{-5} mbar. The deposition was carried out using rates of about 0.04 nm s^{-1} and was monitored in situ by reflection high-energy electron diffraction. Cr_2O_3 layers were subjected to a vacuum annealing process at 750 °C and residual pressure of 10^{-7} mbar directly after growth. This results in an atomically smooth sample surface over ∼200 nm plateaus, with single lattice steps in height at the boundary between plateaus, as verified by atomic force microscopy (Fig. 1d in the main text), as well as high sample

crystallinity (Fig. S2). The thin Pt top layers were magnetron-sputter-deposited at lower temperatures of $\approx$ 100 °C using a higher rate of 0.1 nm s^{-1} to maintain layer continuity. Hall crosses were patterned from the top Pt layers, by SF_6 reactive ion etching around a photoresist mask.

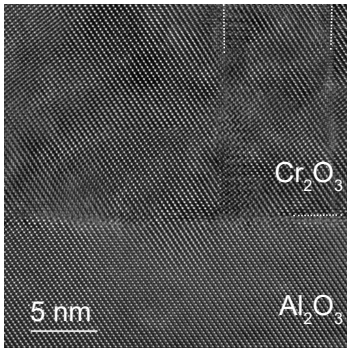

Figure S2: Cross-sectional transmission electron microscopy image of the Cr_2O_3 demonstrating the high crystalline quality of the individual grains. The grain boundaries are highlighted with white dashed lines.

4 Cr_2O_3 surface termination

The Cr_2O_3 surface termination consists of a half-filled layer of Cr atoms, all belonging to the same AF sublattice, as shown schematically in Fig. 1b. This surface termination results from the growth of the Cr_2O_3 crystal in unit steps of Cr-O_3-Cr, with sub-unit steps being energetically unfavorable. The resulting surface magnetization is rigidly linked to the underlying AF order parameter. This picture of the Cr_2O_3 surface has been established in the literature,[5] and is consistent with atomic force microscopy of our sample surface showing atomically smooth terraces bounded by 0.26 nm Cr-O_3-Cr unit steps (Fig. 1d). It is also consistent with our magnetic field data.

It is important to note that sub-unit steps, which would result in a terminal Cr layer that varies between empty, half-filled, and filled, would also give rise to magnetic field contrast,

however the contrast from such steps would be markedly different from our observations in two important ways. First, upon temperature-cycling the sample across T_{crit}, we observe completely uncorrelated domain patterns. If our magnetic signal were due to structural variations in the surface, we would expect to see magnetic contrast at the same locations after temperature cycling, which is not the case. Secondly, the contrast would be between a magnetized surface (for the half-filled configuration) and a non-magnetized surface (for the empty or filled configurations). The sign of the magnetization would still be linked to the underlying AF order parameter, so we would expect to see 3 distinct values of surface magnetization, with some regions positive, some negative, and some zero. The results of our measurements indicate only positive and negative regions, as shown in Fig. 2, and the surface magnetization that we extract from these measurements (which are quantitative by the nature of NV magnetometry) is consistent with a density of electron spins corresponding to a half-filled terminal Cr layer. Our magnetic field observations therefore rule out the possibility of sub-unit steps in the Cr_2O_3 surface.

5 Determination of $\sigma(x, y)$ from 2-D magnetic stray field profiles

We determine the surface moment density profile $\sigma(x, y)$ (Fig. 2b,d) from our measurement of the magnetic field $B_{\mathrm{NV}}(x, y, h_{\mathrm{NV}})$ in the plane at a height h_{NV} above the surface of the film (Fig. 2a) via a Fourier propagation method,[6] which we now describe. We assume a perpendicularly magnetized layer of spins of moment density $\sigma(x, y)$ at the top surface of the film ($z = 0$), and an oppositely magnetized layer at the bottom surface of the film ($z = -d$, with film thickness d). It is convenient to work in Fourier space, where we consider $\tilde{\sigma}(k_x, k_y)$, the two-dimensional Fourier transform of $\sigma(x, y)$ (we will continue to work in real space along the z-axis). Because there are no external time-varying electric

fields or currents, we can define a magnetic scalar potential $\tilde{\phi}(k_x, k_y, z)$ that is the solution to the Laplace equation with boundary conditions set by $\tilde{\sigma}(k_x, k_y)$. Consider first the top layer of spins at $z = 0$. The potential at a height z is found from the moment density by $\tilde{\phi}_{top}(k_x, k_y, z) = \tilde{\phi}_{top}(k_x, k_y, 0)e^{-kz} = \tilde{\sigma}(k_x, k_y)e^{-kz}/2$, where $k = (k_x^2 + k_y^2)^{1/2}$. The magnetic field is then computed from the gradient of $\tilde{\phi}_{top}(k_x, k_y, z)$. Adding the contribution from the bottom layer of spins we thus have the magnetic field in the plane of the NV, $\tilde{\vec{B}}(k_x, k_y, h_{\rm NV}) = -\mu_0 \vec{\nabla}_k(\tilde{\phi}_{top} + \tilde{\phi}_{bottom})$, with in-plane and perpendicular components given by

$$\tilde{B}_{x,y}(k_x, k_y, h_{\rm NV}) = -i\mu_0 k_{x,y} \frac{e^{-kh_{\rm NV}} - e^{-k(h_{\rm NV}+d)}}{2} \tilde{\sigma}(k_x, k_y) \equiv T_{x,y}\tilde{\sigma}(k_x, k_y) \quad (1)$$

$$\tilde{B}_z(k_x, k_y, h_{\rm NV}) = \mu_0 k \frac{e^{-kh_{\rm NV}} - e^{-k(h_{\rm NV}+d)}}{2} \tilde{\sigma}(k_x, k_y) \equiv T_z\tilde{\sigma}(k_x, k_y). \quad (2)$$

We now relate the field projection along the NV axis, $\tilde{B}_{\rm NV}(k_x, k_y, h_{\rm NV})$, to the surface moment density through a single propagator $T_{\rm NV}$:

$$\begin{aligned} \tilde{B}_{\rm NV}(k_x, k_y, h_{\rm NV}) &= \sin(\theta_{\rm NV})\cos(\phi_{\rm NV})\tilde{B}_x + \sin(\theta_{\rm NV})\sin(\phi_{\rm NV})\tilde{B}_y + \cos(\theta_{\rm NV})\tilde{B}_z \quad (3) \\ &\equiv T_{\rm NV}\tilde{\sigma}(k_x, k_y) \quad (4) \end{aligned}$$

Using $T_{\rm NV}$, the moment density profile can be transformed into a magnetic field at a height z from the sample. Moreover, using the inverse propagator a reverse propagation can be performed and the moment density profile can be directly determined from the 2 dimensional field map measured at a distance $h_{\rm NV}$ above the sample.

High frequency components (large k) of the moment density get damped by the exponential factor in the propagator. Conversely, by performing the reverse propagation, high frequency oscillations (including measurement noise) get enhanced. To filter out such high

frequency noise, we introduce a filter function given by a Hanning window[7]

$$W(k) = \begin{cases} 0.5[1 + \cos(\pi\,[k h_{\mathrm{NV}}/2\pi])], & \text{for } k h_{\mathrm{NV}}/2\pi < 1 \\ 0, & \text{for } k h_{\mathrm{NV}}/2\pi > 1, \end{cases} \tag{5}$$

which cuts off frequencies higher than $k_{\mathrm{cutoff}} = 2\pi/h_{\mathrm{NV}}$, motivated by the fact that the NV center can only resolve oscillations with a frequency given by the NV to sample distance h_{NV}.

The magnetic moment density profile can finally be determined from the measured magnetic field map using

$$\sigma(k) = T_{\mathrm{NV}}^{-1}(h_{\mathrm{NV}}, \theta_{\mathrm{NV}}, \phi_{\mathrm{NV}}) W(k) B_{\mathrm{NV}}(k). \tag{6}$$

In order to apply this equation to find the underlying moment density profile, we apply the following procedure. First, we reverse propagate the field using an approximate starting value for h_{NV}, θ_{NV} and ϕ_{NV} to find a moment density $\sigma(x, y)$. From $\sigma(x, y)$ we find the domain boundaries, and assume a uniform moment density within a given domain, $\sigma_{\pm} = \sigma_0\,\mathrm{sign}[\sigma(x, y)]$. We then forward propagate $\sigma_{\pm}(x, y)$ and compare with the original stray field data. Using a least square fitting routine, we then find the values of the NV-to-sample distance ($h_{\mathrm{NV}} = 120\,\mathrm{nm}$), the NV orientation ($\theta_{\mathrm{NV}} = 54\,^{\circ}$, $\varphi_{\mathrm{NV}} = 92\,^{\circ}$) and the moment density ($\sigma_0 = 3\,\mu_{\mathrm{Bohr}}/\mathrm{nm}^2$) that best reproduce the measured magnetic field. The fitted values of h_{NV}, θ_{NV} and ϕ_{NV} are then used for a final back-propagation to generate the moment density profile depicted in Fig. 2b.

6 Surface moment density determined via uniformly magnetized stripes of Cr_2O_3

To confirm the measurement of surface moment density obtained by Fourier propagating the magnetic field of the domain pattern, we additionally patterned a stripe into the Cr_2O_3 film and imaged the stray field of a uniform magnetized film, which we generated by magnetic field cooling.

We structured 1-μm-wide Cr_2O_3 stripes from a 200-nm-thick Cr_2O_3 film coated with 2 nm of Pt. We first fabricated stripe masks using ebeam lithography (30 keV) with a hydrogen silsesquioxane ebeam resist (HSQ, FOX-16 Dow Corning). The pattern was afterwards transferred into the Cr_2O_3 using inductively coupled plasma reactive ion etching (ICP-RIE, Sentech SI 500) for 120 s in an $ArCl_2$ plasma (40 sccm Cl_2, 25 sccm Ar, 1.0 Pa pressure, 400 W ICP power, 100 W RF power with -232 V bias). We removed the etch mask using buffered oxide etch (10:10:1 deionized water, ammonium fluoride, 40 % HF) for 60 s. The etch depth was 250 nm, ensuring that the unmasked Cr_2O_3 film is fully etched through. We also observed a tapering of the sidewalls, which we later included in the stray field calculation.

We model the stray field of a uniformly magnetized Cr_2O_3 film as a stack of two oppositely magnetized ferromagnetic layers, separated by 200 nm, and determine the moment density by a fit of our data to this model. A ferromagnetic film with out of plane anisotropy can be seen as the magnetic counterpart of planar capacitor.[8] For a thin film, this results in a stray field that can be described by a current at the edge of the film

$$B_x(x, h_{\mathrm{NV}}) = \frac{\mu_0 I}{2\pi} \frac{h_{\mathrm{NV}}}{h_{\mathrm{NV}}^2 + x^2} \tag{7}$$

$$B_z(x, h_{\mathrm{NV}}) = \frac{\mu_0 I}{2\pi} \frac{x}{h_{\mathrm{NV}}^2 + x^2}, \tag{8}$$

where the current I is set by the moment density.

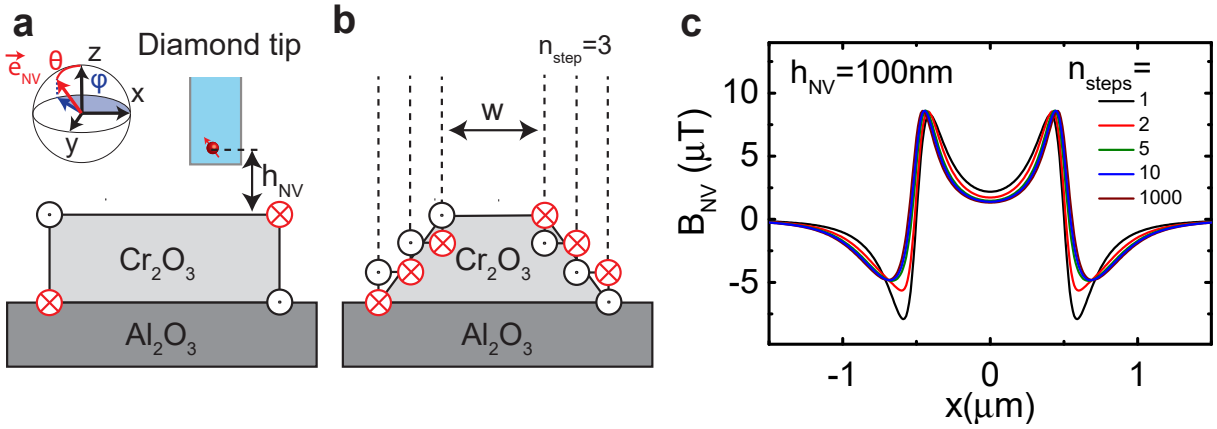

Figure S3: (a) Schematic of a Cr_2O_3 stripe. The magnetic field of the stripe can be calculated as the magnetic field of four currents at the edges. (b) The sidewalls of a tapered stripe are approximated as stairs carrying currents at the edges. (c) Calculated magnetic field of a stripe (width $w = 1\,\mu$m) with tapered sidewalls (45°), at a height $h_{\mathrm{NV}} = 100\,$nm ($\theta_{\mathrm{NV}} = 54°$, $\varphi_{\mathrm{NV}} = 90$). The stray field for different numbers of steps indicates the convergence of this model.

The magnetic stray field of the AF stripes can be described by four such edge currents, as illustrated in Fig. S3a. The stray field is then given by $B_{x,z}^{\mathrm{stripe}} = [B_{x,z}(x - w/2, h_{\mathrm{NV}}) - B_{x,z}(x + w/2, h_{\mathrm{NV}})] - [B_{x,z}(x - w/2, h_{\mathrm{NV+d}}) - B_{x,z}(x + w/2, h_{\mathrm{NV+d}})]$, as depicted in Fig. S3c (black curve).

The etch produced tapered sidewalls to the stripe. We take this tapering of the sidewall into account by decomposing it into n_{steps} steps (see Fig. S3b) and leaving the angle of the sidewall as a fit parameter. The final magnetic field is calculated as a field produced by $4n_{\mathrm{steps}}$ currents. The stray field for an angle of 45° is plotted in Fig. S3c for different n_{steps}, illustrating the convergence of the model. Finally, we fitted this model (where we chose $n_{\mathrm{steps}} = 10$ as a trade-off between calculation time and accuracy of the model), to the measured magnetic field map to precisely determine the NV-to-sample distance and the moment density.

Fitting this model to the stray field of 16 lines perpendicular to the stripes (Fig. S4) yields

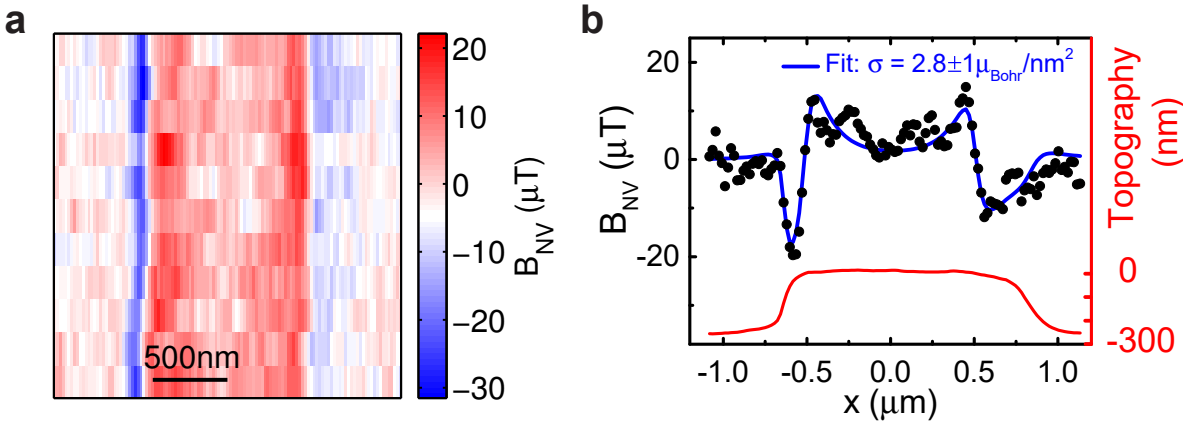

Figure S4: (a) Measured stray field map of the uniformly magnetized stripe. (b) Linecut of the magnetic field (black dots) and topography (red curve) across the stripe. The fitting of 16 linecuts yields an NV-to-sample distance $h_{\mathrm{NV}} = 89 \pm 23\,\mathrm{nm}$ and a moment density of $\sigma = 2.8 \pm 1\,\mu_{\mathrm{Bohr}}/\mathrm{nm}^2$.

a distance of $h_{\mathrm{NV}} = 89 \pm 23\,\mathrm{nm}$ and a moment density of $\sigma = 2.8 \pm 0.7\,\mu_{\mathrm{Bohr}}/\mathrm{nm}^2$. This value confirms the moment density determined via the back-propagation method shown in Fig. 2 in the main text and outlined above.

7 Comparison to stray fields from the surface of bulk, single-crystal Cr_2O_3

Our Cr_2O_3 thin film is a complex system with many structural irregularities due to its granularity. To rule out the possibility that our observations originate from these irregularities, we studied the stray magnetic fields of a bulk, single-crystal Cr_2O_3 sample. We obtained a 5mm x 5mm x 1mm, (0001) oriented, single-crystal Cr_2O_3 sample (MaTecK), which is magnetized in a monodomain state. For uniform magnetization, a flat surface exhibits no stray field. We therefore structured a 200nm-tall stripe into the sample surface as described in section 6 (using only 100 s of etching in this case). The resulting stray magnetic field measured under ambient conditions at room temperature is show in Fig. S5, and is in good agreement

with our model of a uniformly magnetized surface moment density. The estimated surface moment density of $3.8 \pm 1.3\,\mu_{\mathrm{Bohr}}/\mathrm{nm}^2$ is slightly higher than for the thin film, consistent with the higher Néel temperature of bulk Cr_2O_3.

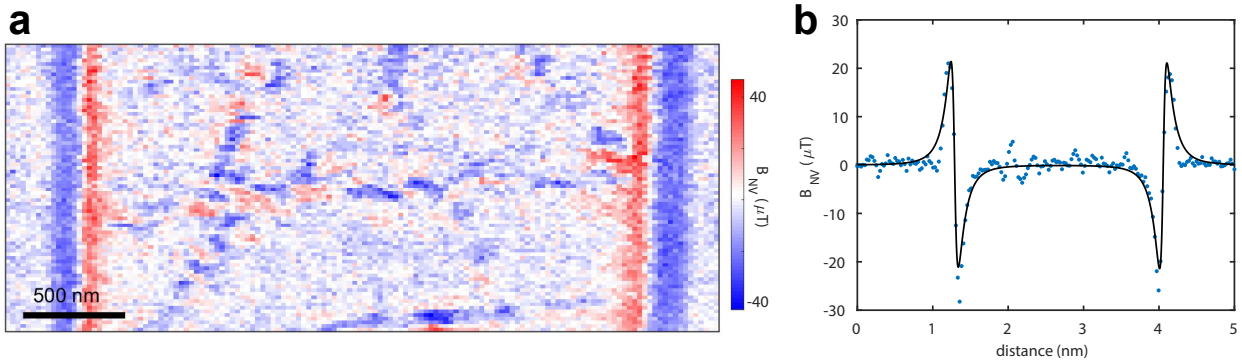

Figure S5: (a) Stray magnetic field from a bulk, single-crystal sample of Cr_2O_3. The (0001) oriented surface is structured with a 200nm-tall stripe. (b) Line cut profile averaged over 80 scan lines. Fit to Cr_2O_3 surface spin model indicates a surface moment density of $3.8 \pm 1.3\,\mu_{\mathrm{Bohr}}/\mathrm{nm}^2$.

8 Determination of $P(T_{\mathrm{crit}})$

The ZOHM measurement of $R_{\mathrm{Hall}}(T)$ (Fig. 3a) indicates the presence of a wide range of critical temperatures in our film. As described in the main text, we determine the distribution of critical temperatures, $P(T_{\mathrm{crit}})$, from a convolution of the single-critical-temperature function $\sigma(\tau) = (1-\tau)^{0.35}\Theta(1-\tau)$, where Θ is the Heaviside step function. In practice, we divide our temperature range into a set of discrete, 0.5 K-wide bins to construct the fit function $R_{\mathrm{Hall}}(T) = \sum_i p_i \sigma(T/T_i)$, and find the fit parameters $\{p_i\}$ that best describe our data. The resulting histogram is shown in Fig. 3b.

9 Temperature calibration

The measurements reported here were taken with 3 different temperature controlled apparatuses, which must be calibrated to each other. The ZOHM measurement of $R_{\mathrm{Hall}}(T)$ (Fig. 3a) is taken as the reference measurement, from which the critical temperature distribution $P(T_{\mathrm{crit}})$ is determined, as above. The DFC measurement (Fig. 4a-b) was taken with a different peltier heater and temperature sensor, so the temperature is shifted in order to fit the data to the theoretical curve (which is derived from $P(T_{\mathrm{crit}})$). Finally, all of the NV magnetometry data were taken with a third peltier stage and thermistor, which we also calibrate to the ZOHM measurement of $R_{\mathrm{Hall}}(T)$. To do so, we use the NV magnetometry measurement of domain cross-correlation under temperature cycling (Fig. 4d), which has a sharper temperature dependence than the measurement of magnetization vs. temperature (Fig. 3a), and from which we determined a temperature shift of $0.5(1)\,\mathrm{K}$. We thus shifted the temperature of our NV magnetometry measurements by $0.5\,\mathrm{K}$, so that the turn-on temperature for the cross correlation signal aligns with the simulation based on $P(T_{\mathrm{crit}})$ (Fig. 4d).

10 Granular model of ordering dynamics

To model the ordering dynamics of our thin film, we introduce a framework based on an ensemble description of fundamental indivisible AF entities, which we attribute to crystallographic grains.[9] The order parameter within a given grain is uniform and is determined by a combination of external fields and exchange coupling to neighbouring grains. Because the size of a grain defines its magnetic anisotropy energy, and therefore its thermal stability, the critical temperature at which a grain undergoes the PM-AF phase transition is size dependent and falls within the distribution shown in Fig. 3b, with the largest grains having the highest T_{crit}. As the film is cooled through this temperature distribution, the grains therefore order sequentially by size, with the order parameter L of each grain taking a value of ± 1. We

describe the ordering outcome for each grain probabilistically as detailed below, with a single phenomenological quantity P_E parameterising the strength of the exchange coupling between grains. By simulating $\langle L \rangle$ for a sufficiently large sample size, we can model the expected behaviour of our film in both the DFC and domain cross-correlation measurements.

10.1 Methodology

Given a set of grains $\{i\}$ ordered by inverse critical temperature $\{T^i_{\text{crit}}\}$, and having areas $\{A^i\}$, we determine the order parameter L^i of grain i based on two possible influences, as follows. First, if grain i has antiferromagnetically ordered neighbors, then with probability P_E, L^i is determined by exchange coupling to neighboring grains, in which case L^i is selected by a random draw, weighted such that the expectation value of L^i is equal to the average order parameter of the neighboring grains. Alternatively, with probability $1 - P_E$, or if all neighboring grains are still paramagnetic, L^i is not determined by exchange coupling. In this case, L^i is assigned to $+1$ with probability $(\eta^i + 1)/2$, and to -1 otherwise. The introduction of η^i allows for the possibility of an externally applied field that biases the ordering in one direction or the other. η^i can therefore take on any value in the range $[-1, +1]$, with $\eta^i = 0$ corresponding to no applied field. In the DFC experiment, η is set to $+1$ initially and is flipped to -1 at temperature T_{switch}. In the domain cross-correlation experiment, $\eta = 0$ always. An example of cooling 20 grains with $P_E = 1$ and $\eta = 0$ is shown in Fig. S6(a-c).

With the resulting $\{L^i\}$ and $\{T^i_{\text{crit}}\}$ from such a simulation, we calculate the observable quantities $\langle L \rangle$ and $B_{\text{NV}}(x, y, h_{\text{NV}})$.

10.2 Differential Field Cooling

In the differential field cooling experiment, the external field is initially set to a high value ($\eta_{\text{high}} = 1$) and then is reversed at T_{switch} ($\eta(T > T_{\text{switch}}) = \eta_{\text{low}} = -1$). Measuring the

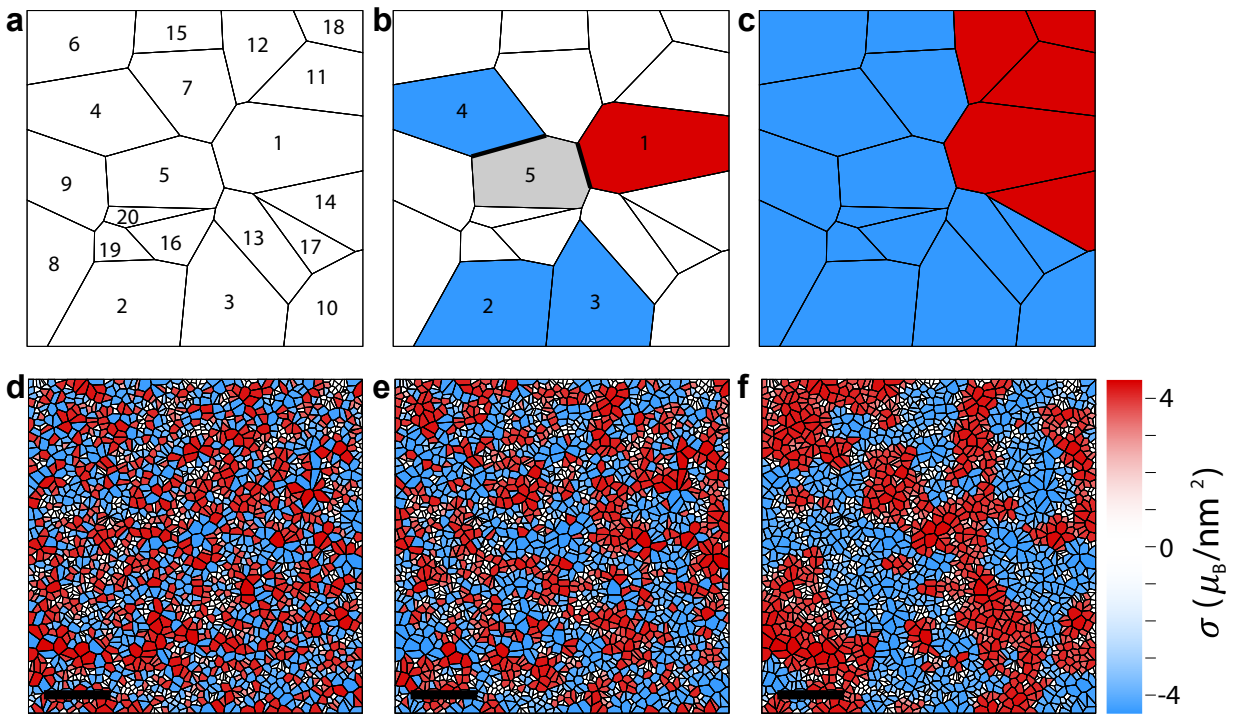

Figure S6: **Magnetic ordering of grains.** (a-c) Ordering of 20-grain mesh for $P_E = 1$, $\eta = 0$. (a) Voronoi mesh based on 20 randomly selected points, with grains ordered by largest to smallest area. Above T_{crit} all grains are in a paramagnetic state. (b) After some cooling, grains 1-4 have formed 3 distinct nucleation spots, with $L^{1,2,4}$ selected randomly, while L^3 is determined from exchange coupling to grain 2. As the temperature is lowered through T^5_{crit}, L^5 is determined from the average of L^1 and L^4, weighted by border length (thick black lines). (c) After further cooling, the sample has completely transitioned to the AFM state, and the 3 initial nucleation spots have spread to form 2 domains. (d-f) Simulation of zero-field cooling on a random mesh with (d) $P_E = 0.0$, (e) $P_E = 0.5$, and (f) $P_E = 1.0$, after cooling to a temperature of 294.15 K. In the case of strong exchange coupling between grains, the zero-field cooled magnetization pattern closely resembles the domain images observed in the experiment, whereas for weaker exchange coupling the simulated domains are more fragmented. (Scale bars: 0.5 µm).

anomalous Hall resistance over the area of the Hall cross yields the average order parameter $\langle L \rangle$. We model this process on set of grains $\{i\}$, as outlined above, but do not make any assumption about the spatial layout of the grains. Instead, we use the macroscopic properties of the film, namely the fractional ordered area and the average order parameter at the time of ordering of grain i, as a statistical average description of the neighbours of grain i. Thus,

the order parameter of grain i becomes:

$$\langle L^i \rangle = P_E \frac{\sum_{j<i} L^j A^j}{A_{tot}} + \left[1 - P_E \frac{\sum_{j<i} A^j}{A_{tot}} \right] \eta^i, \tag{9}$$

where A_{tot} is the total sampled area. In the limit of large number of grains, the average order parameter is given by

$$\langle L \rangle (T_{\text{switch}}, P_E) = \eta_{\text{low}} + (\eta_{\text{high}} - \eta_{\text{low}}) \frac{A_{\text{AF}}(T_{\text{switch}})}{A_{\text{tot}}} e^{P_E \left(1 - \frac{A_{\text{AF}}(T_{\text{switch}})}{A_{\text{tot}}}\right)}, \tag{10}$$

where $A_{\text{AF}}(T_{\text{switch}})$ is the ordered area at the time of switching:

$$A_{\text{AF}}(T_{\text{switch}}) = \int_{T_{\text{switch}}}^{\infty} \tau_A(T_{\text{crit}})\, dT_{\text{crit}}. \tag{11}$$

This result is shown by the solid curves in Fig. 4b for several values of P_E. In the limit of no exchange coupling, i.e. $P_E = 0$, the order parameter of grain i is determined by η^i, so that the average order parameter is found simply by integrating over the ordered area at the time of switching:

$$\langle L \rangle (T_{\text{switch}}, P_E = 0) = \eta_{\text{low}} + (\eta_{\text{high}} - \eta_{\text{low}}) \frac{A_{\text{AF}}(T_{\text{switch}})}{A_{\text{tot}}}. \tag{12}$$

On the other hand, with the addition of exchange coupling between grains, the area that orders before the switch (η_{high}) influences the ordering of subsequent grains, resulting in an effectively larger area experiencing the η_{high} stimulus. The comparison in Fig. 4b between the experimental results and the analytic expression in Eq. 10 indicates a high degree of exchange coupling between grains, with $P_E = 0.989$.

10.3 Domain cross-correlation under temperature cycling

We further investigated the effects of exchange coupling microscopically via domain cross correlation under temperature cycling. In this case, to fully simulate the experiment we require a real-space grain configuration, so we begin by defining a random Voronoi mesh that approximates the grain size distribution in our film. Furthermore, we assign a critical temperature to each grain such that the area-weighted distribution of critical temperatures for the mesh follows the distribution in Fig. 3b, and such that $T^i_{\mathrm{crit}} > T^{i+1}_{\mathrm{crit}}$. Since we know exactly the state of each grain's neighbours, we can assign the order parameter of grain i directly instead of using the macroscopic film properties. Thus, when L^i is determined by exchange coupling (probability P_E), we assign L^i based on the average order parameter of the surrounding grains, weighted by border length: $L^i = \mathrm{sign}\left[\sum_{j\in\mathcal{N}^i} L^j b^{i,j}\right]$, where $\mathcal{N}^i$ is the set of neighbours of grain i and $b^{i,j}$.

To simulate the experiment on the mesh, we first cool with $\eta = 0$ to a measurement temperature T_{start} and record $\{L^i_{\mathrm{init}}\}$. Then, we heat to a temperature T_{cycl}, resetting L for all grains with $T_{\mathrm{crit}} < T_{\mathrm{cycl}}$. Finally, we again cool to T_{start} and record $\{L^i_{\mathrm{final}}\}$. We then calculate $B_{\mathrm{NV}}(x, y, h_{\mathrm{NV}})$ resulting from $\{L^i_{\mathrm{init}}\}$ and $\{L^i_{\mathrm{final}}\}$ (via Fourier propagation, as above), and correlate the initial and final magnetic field images, just as is done in the the experiment:

$$C = \frac{\int B^{\mathrm{init}}_{\mathrm{NV}}(x,y)\, B^{\mathrm{final}}_{\mathrm{NV}}(x,y)\, dxdy}{\left(\left[\int (B^{\mathrm{init}}_{\mathrm{NV}}(x,y))^2\, dxdy\right]\left[\int (B^{\mathrm{final}}_{\mathrm{NV}}(x,y))^2\, dxdy\right]\right)^{1/2}}. \tag{13}$$

This correlation function effectively minimizes the contribution of any parts of the film that are not ordered at T_{start}. Due to experimental constraints, for these experiments $T_{\mathrm{start}} = 299.5\,\mathrm{K}$, which is within the range of T_{crit} for our film. Therefore, a significant fraction of the film is not ordered at T_{start}. We take this into account in our simulations via the local T^i_{crit} values, by assigning a local magnetic moment density to each grain, $\sigma^i = \sigma_{\mathrm{sat}}(1 - (T_{\mathrm{start}}/T^i_{\mathrm{crit}}))^\beta$, where $\sigma_{\mathrm{sat}} = 15\,\mu_B/\mathrm{nm}^2$ and $\beta = 0.35$.

At the end of the simulation we thus have the initial and final order parameter and the local moment density for each grain, from which we calculate the field in the plane of the NV center, using the Fourier propagation method described above. We then take the simulated fields before and after temperature cycling, add Gaussian random noise at the level of the field measurement noise in our experiment, and calculate C as in Eq. 13. The simulated value of $C(T_{\mathrm{cycl}})$ is plotted for $P_E = 0.0, 0.33, 0.67, 1.0$ in Fig. 4d.

References

(1) Rondin, L.; Tetienne, J.-P.; Hingant, T.; Roch, J.-F.; Maletinsky, P.; Jacques, V. *Rep. Prog. Phys.* **2014**, *77*, 56503, DOI: 10.1088/0034-4885/77/5/056503.

(2) Appel, P.; Neu, E.; Ganzhorn, M.; Barfuss, A.; Marietta,; Batzer,; Gratz, M.; Tschöpe, A.; Maletinsky, P. *Rev. Sci. Inst.* **2016**, *87*, 063703, DOI: 10.1063/1.4952953.

(3) Schoenfeld, R. S.; Harneit, W. *Phys. Rev. Lett.* **2011**, *106*, 030802, DOI: 10.1103/PhysRevLett.106.030802.

(4) Kosub, T.; Kopte, M.; Radu, F.; Schmidt, O. G.; Makarov, D. *Phys. Rev. Lett.* **2015**, *115*, 097201, DOI: 10.1103/PhysRevLett.115.097201.

(5) He, X.; Wang, Y.; Wu, N.; Caruso, A. N.; Vescovo, E.; Belashchenko, K. D.; Dowben, P. A.; Binek, C. *Nat. Mater.* **2010**, *9*, 579–585, DOI: 10.1038/nmat2785.

(6) Meyer, E.; Hug, H. J.; Bennewitz, R. *Scanning Probe Microscopy*; Springer-Verlag Berlin Heidelberg, 2004; DOI: 10.1007/978-3-662-09801-1.

(7) Roth, B. J.; Sepulveda, N. G.; Wikswo, J. P. *J. Appl. Phys.* **1989**, *65*, 361–372, DOI: 10.1063/1.342549.

(8) Hingant, T.; Tetienne, J.-P.; Martínez, L. J.; Garcia, K.; Ravelosona, D.; Roch, J.-F.; Jacques, V. *Phys. Rev. Appl.* **2015**, *4*, 014003, DOI: 10.1103/PhysRevApplied.4.014003.

(9) Kosub, T. Ferromagnet-Free Magnetoelectric Thin Film Elements. Ph.D. thesis, TU Chemnitz, Chemnitz, 2016.